Remote Sensing of Environment 288 (2023) 113497

Contents lists available at ScienceDirect

Remote Sensing of Environment

journal homepage: www.elsevier.com/locate/rse

Shape from spectra

Nimrod Carmon [a,*], Alexander Berk [b], Niklas Bohn [a], Phillip G. Brodrick [a], Jeff Dozier [c], Margaret Johnson [a], Charles E. Miller [a], David R. Thompson [a], Michael Turmon [a], Charles M. Bachmann [d], Robert O. Green [a], Regina Eckert [a], Elliott Liggett [a], Hai Nguyen [a], Francisco Ochoa [e], Gregory S. Okin [e], Rory Samuels [f], David Schimel [a], Joon Jin Song [f], Jouni Susiluoto [a]

[a] Jet Propulsion Laboratory, California Institute of Technology, Pasadena, CA, 91109, United States of America
[b] Spectral Sciences Inc., 4 Forth Avenue, Burlington, 01803-3304, MA, United States of America
[c] Bren School of Environmental Science & Management, University of California, Santa Barbara, City Two, 93106, United States of America
[d] Chester F. Carlson Center for Imaging Science, Rochester Institute of Technology, Rochester, NY, United States of America
[e] Department of Geography, University of California, Los Angeles, CA, United States of America
[f] Statistical Science, Baylor University, One Bear Place 97140, Waco, 76798, TX, United States of America

ARTICLE INFO

Edited by Jing M. Chen

MSC:
0000
1111

Keywords:
Topography
Atmospheric correction
Topographic correction
Reflectance retrievals
Imaging spectroscopy
Surface biology and geology
Orbital imaging spectroscopy

ABSTRACT

We introduce a new unified atmospheric–topographic correction approach that estimates surface geometry directly from the radiance measurement. Surface topography influences the at-sensor radiance measurement, making precise topography modeling critical in applications like vegetation or snow studies in mountainous terrain. Currently, elevation maps are used to derive topographic variables such as the slope and sky-view factor. This process is error-prone since static global digital elevation models do not generally achieve the accuracy required, and even minor mismatches in spatial resolution can introduce significant artifacts in downstream processing. Here we demonstrate that it is possible to estimate topographic parameters directly from spectral data, ensuring perfect physical consistency, temporal coincidence, and spatial alignment. We present experiments estimating topographic slope in two scenes in Southern California, with data from NASA's Next Generation Airborne Visible/Near Infrared Imaging Spectrometer (AVIRIS-NG). We compared our radiance-based estimates against high-resolution lidar datasets. Our initial validation result showed a correlation of $R^2 = 0.864$ ($n = 160$) over the homogeneous surface of Beckman Auditorium's cone-shaped roof on the Caltech campus in Pasadena, California. We then validate the model over a larger study site near Santa Clarita, California, finding $R^2 = 0.923$ ($n = 40,000$) in a 350×350 m area. The accuracy of our model estimates, combined with its systematic advantages over the alternative, show the potential of the approach for use in both airborne campaigns and orbital missions.

1. Introduction

Earth-observing imaging spectrometers sensitive to the Visible to ShortWave InfraRed (VSWIR) spectral range measure the solar radiation reflected from Earth's surface and atmosphere. These high spatial and spectral resolution measurements can be used to find the surface's reflectance and characterize materials based on their spectral signatures (Clark and Rencz, 1999). Traditionally operated from airborne platforms, these measurements have been used for local or regional surveys, supporting Earth science investigations and resource exploration activities for more than three decades (Green et al., 1998). The many scientific achievements of this technology, as well as recent advances in instrument design, computing power, and analysis techniques, have led to new orbital missions with global coverage, including already operational instruments such as PRISMA (Cogliati et al., 2021), EnMAP (Guanter et al., 2015) and EMIT (Raiho et al., 2022), as well as future missions from NASA – Surface Biology and Geology (SBG) and ESA – Copernicus Hyperspectral Imaging Mission (CHIME).

SBG and CHIME will provide measurements to be used by multiple scientific disciplines, as recommended by the 2017 Earth Science Decadal Survey (Thompson et al., 2020b; Rast et al., 2021). These include applications to soil and minerals, agriculture and ecology, snow and ice, and aquatics, among others (Stavros et al., 2022). Each of these scientific applications uses empirical and physical models

* Corresponding author.
E-mail address: nimrod.carmon@jpl.nasa.gov (N. Carmon).

https://doi.org/10.1016/j.rse.2023.113497
Received 30 September 2022; Received in revised form 30 January 2023; Accepted 2 February 2023
Available online 14 February 2023

to relate application-relevant quantities of interest to the reflectance (Cawse-Nicholson et al., 2021). These biogeophysical attribute maps are then used to support investigation of relevant questions, and to feed into larger-scale temporal-based analyses (Connelly et al., 2021). A critical step that undergirds all of these products is the inversion of the at-sensor radiance measurement to surface reflectance using 'atmospheric correction' procedures (Doxani et al., 2018).

The objective of atmospheric correction is to invert radiance to reflectance by compensating for the attenuation of the measured signal by aerosols and atmospheric gases, as well as for illumination and observation geometry (Richter and Schläpfer, 2019). Whereas observation and illumination (solar) geometry is known from the measurement process, the conditions of the atmosphere and the surface at the time of acquisition (their states) are unknowns and must be estimated for every pixel in the image. Usually, the unknown atmospheric state is parameterized by two variables, the aerosol optical thickness (AOT) and the water vapor concentration, while the surface state is parameterized by the pixel-level surface reflectance spectral signature (Carmon et al., 2020).

Widely used atmospheric correction implementations such as ATCOR (Richter and Schläpfer, 2019), ATREM (Thompson et al., 2015), ACORN (Miller, 2002), and FLAASH (Perkins et al., 2005) all use a sequential approach where first the atmospheric state is estimated, followed by a reflectance inversion given the retrieved atmospheric parameters. This approach performs well for flat homogeneous terrains and clear sky where the observation conditions are close to ideal. In contrast, more challenging conditions including rugged terrains and high atmospheric loading, will increase the magnitude of coupling effects of atmosphere and surface signals, reducing the accuracy of the inversion and increasing the uncertainty of the reflectance estimates (Gao et al., 2009). Hence, errors in estimating the atmospheric state will propagate downstream into the reflectance and follow through into the biogeophysical maps, reducing the scientific value of the measurement (Thompson et al., 2020a).

One class of first-order factors that affects atmospheric correction and is commonly neglected in operational reflectance products is topographic effects (Dozier, 2021). They influence the measured radiance by changing the illumination pattern onto the surface of each pixel. For flat terrain, all pixels in the scene are equally illuminated by the global flux, the sum of the direct and diffuse solar downwelling irradiance. In rugged and mountainous terrains, the orientation of the surface relative to the sun scales only the direct solar illumination, changing the composition of the global flux. Because the direct and diffuse illumination have vastly different spectral shapes and are influenced by different atmospheric constituents, this effect is significant and must be accounted for in such environments to reduce uncertainty in reflectance estimates (Carmon et al., 2022).

Accounting for topographic effects in reflectance retrievals can be done in two different ways. One commonly used approach is a sequential method where first the reflectance is estimated without accounting for topography, and then, a 'topographic correction' procedure, usually based on spatial statistics, is applied to the reflectance map (Soenen et al., 2005). A less common approach, first introduced in ATCOR's 'Rugged Terrain' program, is to incorporate topographic effects directly in the initial radiance inversion (Jia et al., 2020). This unified atmospheric–topographic correction scales the direct component of the solar illumination appropriately, removing the influence of topography from the reflectance estimates directly in the inversion, based on physics. Recent work showed that the reflectance estimates from a unified approach are more decorrelated from topography, indicating that these estimates are closer to a terrain invariant, intrinsic reflectance signatures (Carmon et al., 2022). Still, both approaches require maps of topographic parameters calculated based on an auxiliary elevation dataset.

Data fusion of multiple datasets measured by different instruments always introduces uncertainty in the combined product (Nguyen et al., 2012). Specifically for topographic effects, the use of elevation maps and their derivatives in the atmospheric correction procedure can lead to large errors, originating in instrument noise, mismatch in spatial resolutions and co-registration, and from the temporal gap between the two measurements (Dozier et al., 2022). Moreover, while commonly available elevation products are based on digital elevation models (DEMs) which remove features from the surface, the radiance measurements observe the surface as-is, including features above the ground level.

This work overcomes these problems with a methodology to extract topographic information directly from the radiance measurement, providing perfect spatial and temporal alignment with the radiance. Our algorithm is based on a new implementation of an enhanced radiance model that incorporates topographic effects into the initial radiance inversion, and using an optimal estimation (OE) framework, solves for surface reflectance, atmosphere, and topographic conditions, simultaneously.

In the following we describe our formulation of the forward model (Section 2.1) and include a detailed description of the topographic effects implemented in the radiance equation (Section 2.1.1). We describe three experiments designed to evaluate the performance of our model against reference datasets, including an initial validation in an urban scene (Section 4.1) and two experiments in a wilderness scene for airborne (Section 4.2.1) and orbital (Section 4.2.2) spatial resolutions. Our experiments show excellent agreement between our radiance-based topography estimates and the lidar-based maps in both scenes, with smaller errors compared to the globally available NASA DEM (JPL, 2020). Finally, we discuss the advantages of this approach over using auxiliary elevation datasets and suggest further enhancements to include not only topographic effects, but also bidirectional reflectance distribution function (BRDF) models within the initial atmospheric correction procedure.

2. Method

Our approach for estimating topographic variables from radiance measurements incorporates an optimization based atmospheric correction algorithm that treats topographic variables as unknowns and estimates their values from the measurement using nonlinear least squares. We use radiance measurements from the AVIRIS-NG instrument, where each spatial pixels has $c = 425$ spectral channels in the VSWIR spectral range. This inversion strategy is based on optimal estimation techniques where for each pixel we fit the at-sensor radiance measurement $\boldsymbol{y} \in \mathbb{R}_{+}^{c}$ using a forward model $f(.)$, solving for the state vector $\boldsymbol{x}$. The state vector $\boldsymbol{x}$ holds all unknown quantities to be simultaneously estimated during the optimization, including parameters for surface reflectance, atmosphere, and topography, i.e., $\boldsymbol{x} = [\boldsymbol{x}_{rfl}, \boldsymbol{x}_{atm}, \boldsymbol{x}_{geom}]$. The forward model maps between the state space and the measurement space, i.e., $f(\boldsymbol{x}) = \boldsymbol{y}$, and the objective is to find $\hat{\boldsymbol{x}}$, the best solution for the state vector given the measurement. Table 1 summarizes our notation conventions and symbols.

2.1. The forward model

The radiance measurement at the sensor arises from the interaction of the solar irradiance $\boldsymbol{e}_0$ with Earth's atmosphere and surface. Atmospheric gases and suspended particles interact with passing radiation by absorption, reflection, and scattering. To capture these effects, atmospheric radiative transfer models (RTMs) are used to map between the unknown conditions of the atmosphere and their radiative transfer effects on the measurement. The materials on the surface have unique absorption and scattering traits, which absorb and reflect the incoming radiation based on the materials' spectral features and physical structure. Finally, topography and illumination geometry alter the amount and spectral balance of downwelling illumination.

Table 1
Notation conventions. Boldface lowercase indicates vectors, and boldface uppercase indicates matrices. Non-bold lowercase indicates scalars and functions. We treat vectors as columns for matrix algebra.

Symbol	Description
$\boldsymbol{y}$	At-sensor radiance
$\boldsymbol{x}$	Complete state vector, $\boldsymbol{x} = [\boldsymbol{x}_{rfl}, \boldsymbol{x}_{atm}, \boldsymbol{x}_{geom}]$
$\boldsymbol{x}_{rfl}$	Pixel-level reflectance state vector
$\boldsymbol{x}_{atm}$	Atmospheric RTM state vector
$\boldsymbol{x}_{geom}$	Topographic/geometric state vector
$\hat{\boldsymbol{x}}$	State vector at the solution
f	Forward model, a vector-valued function mapping $\boldsymbol{x}$ to $\boldsymbol{y}$
h	Pixel-level linear mixture reflectance model
g	Atmospheric radiative transfer model
$\boldsymbol{e}_o$	Solar irradiance at top of atmosphere
$\boldsymbol{e}_g$	The global, direct plus diffuse, solar irradiance illumination
$\boldsymbol{l}_{obs}$	Modeled radiance at-sensor
$\boldsymbol{l}_{path}$	Path Radiance
$\boldsymbol{s}$	Spherical albedo at bottom of atmosphere
$\boldsymbol{\rho}_b$	Background surface reflectance
$\boldsymbol{t}^{\downarrow}_{dir}$	Downwelling direct transmittance
$\boldsymbol{t}^{\downarrow}_{dif}$	Downwelling diffuse transmittance
$\boldsymbol{t}^{\uparrow}_{total}$	Total, direct plus diffuse, upwelling transmittance
$\boldsymbol{\rho}_t$	Target pixel reflectance
μ_{TOA}	Cosine of the top of atmosphere solar zenith angle
μ_{ϕ}	Cosine of the angle between the normal to the surface and the sun
μ_{sv}	Sky-view factor
μ'_{ϕ}	Terrain illumination intensity factor

In this work, we implement the effect of three topographic variables: topographic slope, sky-view factor, and scene reflection intensity. Although we label these variables as if they were specific geometric properties, their optimal values could change due to other physical phenomena that cause similar spectral effects. So while these variables give a mathematical framework for describing physically-realistic changes in radiance, we caution against interpreting them directly as geometric properties.

The forward model designed and implemented in our approach incorporates a scaling coefficient on the direct flux, μ_{ϕ}, a scaling coefficient on the diffuse downwelling flux, μ_{sv}, and a scaling coefficient accounting for the illumination intensity on adjacent reflecting terrain, μ'_{ϕ}, reflecting the influence of the three topographic variables described above. The radiance equation is:

$$\boldsymbol{l}_{obs} = \boldsymbol{l}_{path} + \frac{\boldsymbol{e}_o \pi^{-1}}{1 - \boldsymbol{s}\boldsymbol{\rho}_b}(\mu_{\phi}\boldsymbol{t}^{\downarrow}_{dir} + \mu_{sv}\mu_{TOA}\boldsymbol{t}^{\downarrow}_{dif} + (1-\mu_{sv})(\mu'_{\phi}\boldsymbol{t}^{\downarrow}_{dir} + \mu_{TOA}\boldsymbol{t}^{\downarrow}_{dif})\boldsymbol{\rho}_b)\boldsymbol{\rho}_t\boldsymbol{t}^{\uparrow}_{total} \quad (1)$$

where $\boldsymbol{e}_0$ is the extraterrestrial solar irradiance at top of atmosphere, $\boldsymbol{l}_{path} = \boldsymbol{e}_o\pi^{-1}\mu_{TOA}\boldsymbol{\rho}_a$ is the atmospheric path radiance, with $\boldsymbol{\rho}_a$ being the atmospheric reflectance. $\boldsymbol{s}$ is the spherical albedo at bottom of atmosphere, $\boldsymbol{t}^{\downarrow}_{dir}$ is the direct downwelling transmittance, $\boldsymbol{t}^{\downarrow}_{dif}$ is the diffuse downwelling transmittance, and $\boldsymbol{t}^{\uparrow}_{total}$ is the total, direct and diffuse, upwelling transmittance. μ_{ϕ} is the cosine of the instantaneous zenith angle, and μ_{TOA} is the top of atmosphere solar zenith angle. μ_{sv} is the sky view factor, $\boldsymbol{\rho}_b$ is a generalized background reflectance, μ'_{ϕ} is the generalized illumination of adjacent pixels reflecting towards the target, and $\boldsymbol{\rho}_t$ is the pixel-level reflectance of the target pixel.

This radiance equation implements the effects of topography using the three topographic parameters captured in the geometry state vector; $\boldsymbol{x}_{geom} = [\mu_{\phi}, \mu_{SV}, \mu'_{\phi}]$, holding free parameters for the topographic slope, sky-view factor and scene reflection intensity. For clarity, we describe and motivate the use of these three variables in the model and illustrate the underlying physics governing them.

2.1.1. Topography

The μ_{ϕ} variable scales the direct solar flux onto the target pixel and is the strongest radiative effect in the radiance equation. Traditionally, μ_{ϕ} is known to account for the effective solar zenith angle between a surface normal direction and the Sun's direction, capturing the radiative effect of topographic slope. Large angles originating from high slopes facing away from the solar direction, lead to each solid angle of solar radiance falling on a larger area of terrain, reducing the direct irradiance on the surface. Small angles, occurring when the surface normal is close to the solar direction, concentrate sunlight on smaller surface areas and increase the magnitude of the direct solar illumination.

In fact, two other geometric/topographic phenomena would result in the same radiative effect on the radiance equation (Fig. 1). First, shadows cast from outside the pixel would effectively reduce the amount of direct illumination onto the pixel. These shadows could completely obstruct the direct solar illumination on the entire pixel, as in the case of high topography surrounding a narrow valley, or could be cast only on a partial area of the pixel, such as in high-texture scenes. Second, the micro-topography and texture of the objects within the pixel, such as tree canopies, would also lead to sub-pixel shadows, reducing the magnitude of the direct illumination. These effects are traditionally referred to as geometric scattering in bidirectional reflectance distribution function (BRDF) models.

The influence of μ_{ϕ} on the modeled radiance allows this parameter to be estimated from the data itself. μ_{ϕ} changes the magnitude of the direct illumination onto the surface, and accordingly, the magnitude of the reflected signal. But it also changes the balance of direct and diffuse illumination, which modifies the spectral shape. Fig. 2 illustrates this effect. We simulate measured radiance spectra with a constant 50% surface reflectance, changing only μ_{ϕ}. We then divide this spectrum by a reference radiance, and mean-center the result. This clearly demonstrates that reducing μ_{ϕ} increases the proportion of signal in short wavelengths.

From Fig. 2 it is clear that the effect of μ_{ϕ} has a strong spectral shape, especially in the visible range. This means that not compensating for μ_{ϕ} will not just result in a magnitude shift on the reflectance, but will have a significant effect on the shape of the estimated spectra.

We also model two interrelated second-order topographic effects — the sky-view factor, and scene reflection intensity (Fig. 3). The sky-view factor μ_{sv} is the proportion of the unobscured sky exposed to the surface compared to a full hemisphere of 2π Sr (steradians), where $0 \leq \mu_{sv} \leq 1$. We separate the sky view factors into two types. Type 1 is

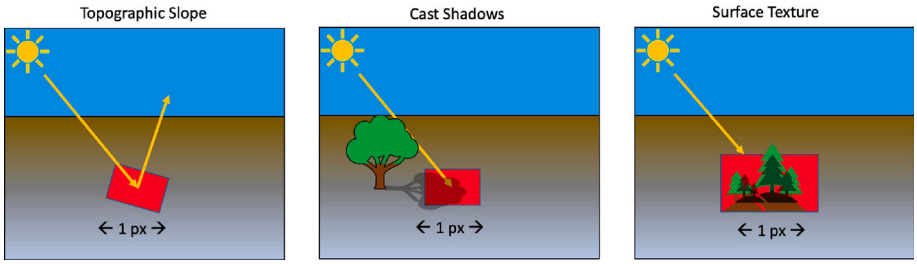

Fig. 1. The three physical phenomena that scale the direct flux arriving on a pre-defined surface area on one pixel (px).

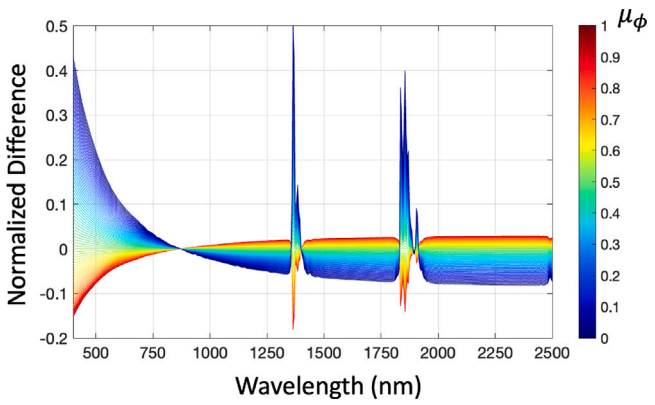

Fig. 2. Normalized differences between true and reference radiance simulations. The effect of changing μ_ϕ has a strong spectral shape effect in the VNIR, and mostly a magnitude effect in the SWIR.

solely due to the pixel's slope (Fig. 3, left panel), leading to intersection of the pixel's attached hemisphere with the horizon, and cannot exceed a value of 0.5, which occurs when the slope is exactly 90°. Type 2 sky view is due to obstruction of the sky by topography and surface features around the target pixel (Fig. 3, center panel). This variable directly scales the downwelling diffuse radiation coming down from the sky onto the pixel.

The complement of the sky-view is the terrain view ($\mu_{terrain} = 1 - \mu_{sv}$), the proportion of the pixel's hemisphere where topography obscures the sky. The topography and surface features around a pixel are illuminated by the sun and may reflect this radiation onto the target. The third free parameter, μ'_ϕ, accounts for radiation coming from adjacent terrain (Wang et al., 2000; Dozier and Frew, 1990). This parameter scales the contribution of the direct illumination reflected from the terrain exposed to the target pixel.

2.1.2. Atmospheric radiative transfer

The atmospheric model maps the atmospheric state to a set of optical atmospheric coefficients required by the radiance equation. It is common to parameterize the unknown state of the atmosphere with two parameters. The first represents the columnar water vapor concentration, captured in the free parameter x_{WV}. The second represents the concentration of aerosols in the atmosphere, where we use the aerosol optical thickness at 550 nm, x_{AOT}, as the free parameter to be estimated. We use the MODTRAN radiative transfer model to calculate the optical coefficients needed by the radiance equation, conditioned on the atmospheric state (Thompson et al., 2018), leading to:

$$g(\boldsymbol{x}_{atm}, \boldsymbol{b}) : [x_{WV}, x_{AOT}] \rightarrow [\boldsymbol{\rho}_a, \boldsymbol{s}, \boldsymbol{t}^{\downarrow}_{dir}, \boldsymbol{t}^{\downarrow}_{dif}, \boldsymbol{t}^{\uparrow}_{total}]$$

where MODTRAN is initialized by the two unknown parameters x_{WV} and x_{AOT}, aggregated in the atmospheric state $\boldsymbol{x}_{atm}$, and $\boldsymbol{b}$ is a vector holding calibration and tuning variables, described below. Each optical coefficient vector has the same dimensions as the measurement vector with each element in the $[0, 1]$ interval.

MODTRAN requires calibration and tuning parameters to estimate the optical atmospheric coefficients. Some of these inputs are known exactly from the measurement process, including the instrument altitude and observation geometry, the surface elevation above sea level (ASL), the date and time of the acquisition, and the solar geometry. Other inputs to MODTRAN are not known exactly but are assigned estimated values consistent with site climatology, including the aerosol type, the atmospheric pressure profile, and concentration values of atmospheric trace gases such as carbon dioxide, ozone, and methane. These state variables, which are not estimated for each pixel, can be lumped into a vector $\boldsymbol{b}$. We acknowledge uncertainties from these assumptions might exist in the end product.

2.1.3. Surface reflectance signature

The radiance model (Eq. (1)) requires a vector of pixel-level surface reflectance $\boldsymbol{\rho}_t$. This reflectance spectrum traditionally captures the hemispherical-directional reflectance factor (HDRF) of the surface for any given pixel. In this work we use a pixel-level reflectance signature model that emphasizes the analysis of mixtures. In this model the pixel-level reflectance is built from a linear mixture of spectral signatures of three endmembers: soil, photosynthetic vegetation (PV) and non photosynthetic vegetation (NPV). We capture the reflectance signature of each endmember using a dimension reduction technique described below that allows us to model each signature using a handful of free parameters. Additionally, we treat the endmember's mixing fractions as unknowns and optimize for them within the inversion. The advantage of this approach is the ability to retrieve not only the pixel-level reflectance signature but also the endmember signatures and fractions underlying it. Finally, the reflectance model maps between the endmember reflectance signatures variables and the mixture fractions to the pixel-level reflectance $\boldsymbol{\rho}_t$ used by the radiance equation, leading to:

$$h(\boldsymbol{x}_{rfl}) : [\boldsymbol{x}_{rfl}, \boldsymbol{x}_f] \rightarrow [\boldsymbol{\rho}_{soil}, \boldsymbol{\rho}_{pv}, \boldsymbol{\rho}_{npv}, \boldsymbol{\rho}_{pixel}]$$

where $\boldsymbol{x}_{rfl}$ holds model parameters for the three endmembers, and $\boldsymbol{x}_f$ holds the relative fractions of each endmember in the mixture. $\boldsymbol{\rho}_{soil}$, $\boldsymbol{\rho}_{pv}$, and $\boldsymbol{\rho}_{npv}$ are the estimated endmember spectral signatures, and $\boldsymbol{\rho}_{pixel}$ is the pixel-level reflectance mixture.

Using these three endmembers promised the reflectance mixture model could capture the majority of spectral shapes that would be encountered in common airborne acquisitions. Moreover, the linear mixture formulation also allows to extrapolate beyond these three surface types and capture pixel level signatures of other materials.

Each endmember signature is reconstructed using a low rank model using a handful of parameters to be estimated in the inversion. We use a large, combined spectral library that consists of approximately 2000 soil, 1000 PV, and 750 NPV in-situ spectra, subset only to spectra measured in drylands. Spectra are a mixture of contact probe with an areal footprint of $1\ cm^2$, and "canopy level" spectra, taken with 20° field of view approximately 1 m above the target. Using Principal Component Analysis (PCA) we developed reflectance reconstruction models for each endmember as described below, to be used by the model.

Next, we calculated a principal component (PC) representation of the dataset allowing us to capture the majority of the variation in the library using a small number of PCs. For each endmember class in the library, we first apply mean centering, and save the spectral mean $\boldsymbol{\mu}$ for later use. We arrange the s mean-centered spectral samples into a matrix $\boldsymbol{D}' \in \mathbb{R}^{c \times s}$, and apply singular value decomposition to find its eigenvectors and eigenvalues. We arrange the eigenvector matrix columns based on the magnitude of variance explained by each one, and save this as a projection matrix $\boldsymbol{V} \in \mathbb{R}^{c \times k}$, where k is the number of PC's. To determine k we set a criterion of 99% total variance explained by the model. We then construct a reflectance model based on the projection matrix that reconstructs reflectance signature using a PC loading vector. In our model, this loading vector is a vector of free parameters that is estimated within the inversion, leading to the form:

$$\boldsymbol{\rho} = \boldsymbol{V}^T \times \boldsymbol{x}_{rfl} + \boldsymbol{\mu}$$

where $\boldsymbol{\rho}$ is the endmember reflectance signature, $\boldsymbol{x}_{rfl}$ is the unknown PC loading vector, and $\boldsymbol{\mu}$ is the spectral mean of the endmember library class.

The outputs from the three endmember PCA models are linearly mixed to allow the pixel-level reflectance model to capture signatures of mixed pixels, resulting in the form:

$$\boldsymbol{\rho}_{pixel} = \sum_{n=1}^{3} x_{f,n}(\boldsymbol{V}_n^T \boldsymbol{x}_{rfl,n} + \boldsymbol{\mu}_n)$$

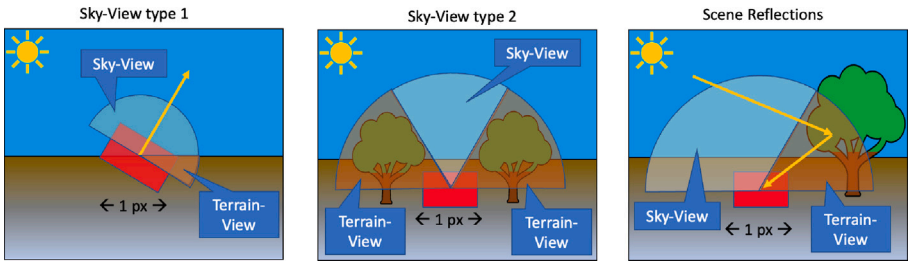

Fig. 3. Sky view factor scales the diffuse downwelling illumination based on the pixel's slope (Type 1), and surface features (Type 2). The complement of the sky-view factor is the terrain-view factor. Topography and objects in the terrain view are illuminated by the sun and may reflect this radiation to the target pixel.

where $_n$ signifies the endmember class and $x_{f,n}$ represents the unknown fraction of the nth endmember in the mixture (Shimabukuro and Smith, 1991).

To summarize, our overall pixel-level reflectance model is a linear composition of endmember reflectance shapes built using underlying PCA models parameterized using a portion of the state vector, linearly mixed by their unknown fractions. This model fits the reflectance in the radiance equation, allowing us to estimate both the pixel-level reflectance, endmember reflectance signatures, and mixing fraction, for any given pixel.

2.2. Optimization

Let $\boldsymbol{y} \in \mathbb{R}_+^c$ be the radiance measurement vector for a single pixel in the image holding the at-sensor radiance for c spectral channels. Instrument noise makes the measured radiance $\boldsymbol{y}$ differ from the true radiance $\boldsymbol{y}^*$. We assume that $\boldsymbol{\gamma}$, the difference between the true and measured radiance, distributes according to a non-biased Gaussian function around the mean with a known diagonal covariance, leading to:

$$\boldsymbol{y} = \boldsymbol{y}^* + \boldsymbol{\gamma}$$

where $\boldsymbol{\gamma} \sim N(0, \boldsymbol{S}_y)$. $\boldsymbol{S}_y$ is a diagonal matrix with elements proportional to the measurement magnitude, scaled according to the signal-to-noise ratio (SNR) of the instrument.

We define $\boldsymbol{x}$, a state vector of free parameters holding all unknown quantities to be estimated. To relate the state vector to the measurement, we use a forward model $\boldsymbol{f}(\boldsymbol{x})$, capturing the physics of the observation process. The forward model $\boldsymbol{f}(.)$ is only a simplified realization of the true physics, and hence results in model discrepancy errors, leading to:

$$\boldsymbol{y} = \boldsymbol{f}(\boldsymbol{x}) + \boldsymbol{\delta} + \boldsymbol{\gamma}$$

where $\boldsymbol{\delta}$ is errors due to model discrepancy, assumed to be Gaussian, i.e., $\boldsymbol{\delta} \sim N(0, \boldsymbol{S}_m)$.

We assume no correlation between instrument noise and model discrepancy, allowing us to formulate our observation model as:

$$\boldsymbol{y} = \boldsymbol{f}(\boldsymbol{x}) + \boldsymbol{\epsilon}$$

where $\boldsymbol{\epsilon}$ is the sum error of instrument noise and model discrepancy, and distributes according to $\boldsymbol{\epsilon} \sim N(0, \boldsymbol{S}_\epsilon)$, where $\boldsymbol{S}_\epsilon = \boldsymbol{S}_y + \boldsymbol{S}_m$.

Our objective is to find the most probable solution for the state vector $\boldsymbol{x}$, given a particular radiance measurement vector $\boldsymbol{y}$. We use Bayes' law of conditional probability that leverages both the measurement likelihood $p(\boldsymbol{y}|\boldsymbol{x})$ and state probability $p(\boldsymbol{x})$ to find the posterior distribution $p(\boldsymbol{x}|\boldsymbol{y})$:

$$p(\boldsymbol{x}|\boldsymbol{y}) = \frac{p(\boldsymbol{y}|\boldsymbol{x})p(\boldsymbol{x})}{p(\boldsymbol{y})} \tag{2}$$

The above terms in the numerator are scalar functions of $\boldsymbol{x}$ and have a Gaussian form. The $\boldsymbol{x}$ state that maximizes Eq. (2) is the maximum a posteriori (MAP) estimate. Maximizing Eq. (2) is equivalent to minimizing its negative log, simplifying the formulation. By taking twice the negative log of the numerator in Eq. (2) and removing terms not a function of $\boldsymbol{x}$, the objective function arises:

$$c(\boldsymbol{x}) = (\boldsymbol{y} - \boldsymbol{f}(\boldsymbol{x}))^T \boldsymbol{S}_\epsilon^{-1} (\boldsymbol{y} - \boldsymbol{f}(\boldsymbol{x})) + (\boldsymbol{x} - \boldsymbol{x}_a)^T \boldsymbol{S}_a^{-1} (\boldsymbol{x} - \boldsymbol{x}_a)$$

where $\boldsymbol{x}_a$ is the state vector's prior mean, and $\boldsymbol{S}_a$ is its covariance.

We use this cost function as input to a gradient descent nonlinear least squares optimization algorithm designed to minimize the cost w.r.t. $\boldsymbol{x}$. We use a trust region solver, and set a convergence criterion of 1% change in the state, following Rodgers n-form formalism for a nonlinear problem with more measurement points than unknowns (Rodgers, 2000). The converged state, $\hat{\boldsymbol{x}}$, is the mode of the posterior distribution and is used as the solution for this inversion.

3. Experimental design

In the following, we show results of experiments designed to test the radiance based μ_ϕ retrievals against traditional elevation map-based μ_ϕ estimates. We compare our radiance μ_ϕ maps with high resolution lidar derived elevation maps and the moderate resolution SRTM DEM product. Below, we describe the different measurements and preprocessing steps, and include a description of our μ_ϕ calculation applied to elevation datasets.

3.1. Radiance measurements

Radiance measurements were acquired using the AVIRIS-NG airborne imaging spectrometer, built and operated by NASA's Jet Propulsion Laboratory (JPL). AVIRIS-NG is a high signal-to-noise ratio (SNR) pushbroom spectrometer producing radiometrically calibrated radiance cubes with 600 cross-track elements and 425 spectral channels in the visible-to-near-infrared (VSWIR; 350–2500 nm) spectral range. The raw digital number (DN) maps are converted to radiance units using rigorous spectral and radiometric laboratory calibration, and are further fine tuned with a hangar calibration prior to every airborne campaign (Chapman et al., 2019). AVIRIS-NG radiances are georeferenced to a UTM projection on the WGS84 coordinate system where each pixel in the map has an accurate location coordinate on Earth's surface.

3.2. Lidar

Lidar measurements were acquired for the United States Geological Survey (USGS) under the 3D Elevation Program (3DEP), tasked with acquiring nationwide consistent high resolution topographic data. Within this project, the entire Los-Angeles county was measured with an Optech Galaxy 1064-nm topographic laser between 2015 and 2016, operated by Pictometry International Corporation. The instrument was mounted on a Piper Aztec Twin Engine aircraft flying at 725 m above ground level (AGL) to satisfy USGS's requirement of 0.7 m target separation. The raw point cloud product is provided in a NAD83 Zone V coordinate system, with a vertical accuracy better than 19 cm. The instrument's beam divergence was 0.25 mrad, resulting in a ground footprint of approximately 0.2 m on a flat surface. The USGS provides both raw point cloud datasets as well as a processed DEM product.

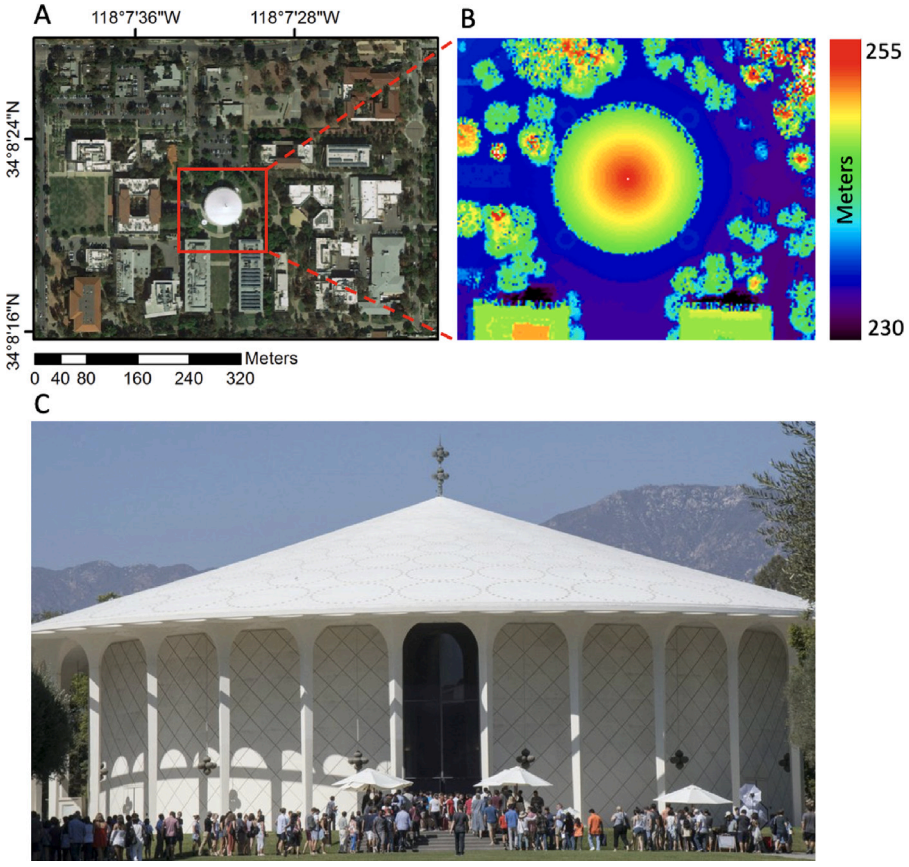

Fig. 4. Beckman Auditorium in the center of the Caltech campus in Pasadena, California. Panel A shows a high resolution airborne RGB image of the campus, indicating the scene is a complex urban environment. Panel B shows a lidar derived elevation map over Beckman Auditorium, where the roof's radius is approximately 25 m. Panel C shows a photograph of Beckman Auditorium taken from the South direction, showing the roof is a symmetric cone with a constant slope angle of approximately 16°, with homogeneous smooth surface of white roof sealing paint.

The DEM was processed from the point cloud excluding non ground level points, rasterized and smoothed, and resampled to 1 m ground sampling distance (GSD).

3.3. SRTM

We acquired DEM based elevation maps from the SRTMGL1 product. SRTMGL1 provides elevation data in a WGS84 Lat/Lon projection, with 1 arcsecond (approximately 30 m) GSD. We obtained a tile over our study area from the land processing data center (LP-DAAC).

3.4. Calculating μ_ϕ on elevation maps

Throughout this work, we calculate μ_ϕ maps based on elevation datasets. Here, we explain our calculation. We start with an elevation map, where the elevation values at each pixel are in units of meters ASL, and the distance between the center of two adjacent pixels, the GSD, is given. We then define a kernel of size 3×3 pixels to calculate the μ_ϕ value of each pixel in the image. Within the kernel's footprint we fit a plane equation to the elevation points, accounting for its elevation differences to the center pixel and for the GSD. By taking the derivative of the plane equation w.r.t. the x and y directions, we find the normal vector to the plane in 3D space. We define a solar vector, constant within a small scene, and take the dot product between the normal to the surface and the solar vector. We normalize by the lengths of each vector, resulting in the cosine of the angle between the two vectors, μ_ϕ.

4. Results

Here, we describe our experimental results by comparing the μ_ϕ maps derived from radiance, to μ_ϕ maps derived from elevation maps, within two study sites. The first study site is in the Caltech campus in Pasadena, where we have identified the Beckman Auditorium's roof as our target for an initial validation experiment. This target has an approximately homogeneous and consistent reflectance, a smooth surface, and its shape is a symmetric cone, ensuring a good representation of different μ_ϕ values. We then continue to evaluate our approach over a much larger scene near Santa Clarita, California, in a site characterized by highly rugged terrain, heterogeneous surfaces, and mixed pixels of soil, dry vegetation, and sparse trees. We run two experiments over this site, where the first is designed to evaluate the performance for a typical airborne resolution and the second for a typical orbital resolution.

4.1. Initial validation over Beckman Auditorium

Beckman auditorium is a large building at the Caltech campus with a unique, 25-m radius symmetric cone roof covered by white roof sealing paint (Fig. 4). This target was selected for validation based on its unique characteristics that simplified both the radiance and lidar data processing. First, the roof's surface is mostly smooth and without texture, reducing the potential influence of textural shadows on the μ_ϕ estimates. The entire roof is painted with a white roof sealing paint, promising consistency in the reflectance signatures for all pixels over the target. Third, the roof is higher than most of its surrounding, limiting potential confusing scattering from neighboring features.

For lidar processing, the smooth and symmetric shape simplified the construction of the elevation map as no surface targets interfere with the estimates. Finally, the roof's symmetric round shape promised a smooth variation of μ_ϕ across the cone to support visual interpretation and validation.

Radiance measurements were acquired by AVIRIS-NG on October 3rd, 2016. The instrument was flying on the Dynamic Aviation King Air B-200 (N53W) aircraft at an altitude of 2.9 km ASL, resulting in a GSD of 2.9 m. We spatially subset the image over our target and processed the radiance into μ_ϕ estimates using our model, resulting with approximately 160 pure roof pixels. At the time of acquisition, the solar azimuth angle was 204° east from north with a solar zenith angle of 42°. A 42° solar zenith angle corresponds to a nominal μ_ϕ of 0.743 for a flat pixel.

Fig. 5 shows an example with the Beckman Auditorium. Panels A and B show the radiance measurements: a true color RGB image with a standard linear contrast stretch and the radiance spectra. Radiances are colored by the lidar-estimated μ_ϕ, illustrating a significant magnitude shift. To isolate the differences in spectral shape, we divide each spectrum by the average roof spectrum, and then mean-center its values. Panels C and D show the result. The sun-facing side (south-east) is more yellow, consistent with the direct solar illumination, and the non sun-facing side is more blue, consistent with the diffuse sky irradiance. Deeper water vapor absorptions in the sun-facing side suggest a longer optical path; the "path radiance" of photons that do not reach the ground is a smaller fraction of sensor-reaching signal.

For validation, we calculated a μ_ϕ map based on the lidar measurements. We obtained the raw point cloud over the scene and manually removed noisy points from the dataset. Next, we rasterized the remaining points, including buildings, vegetation, and ground, to construct the initial DSM elevation map at the lidar nominal GSD of 0.6 m (Fig. 4, Panel B). We then resampled this dataset to the radiance's 2.9 m GSD and coregistered the two images for better alignment.

The results from this analysis are encouraging. Fig. 6 shows a map of the lidar reference μ_ϕ map (upper-left panel), the radiance-derived μ_ϕ prediction (upper-right panel), and a scatter plot of the radiance estimates vs. the lidar estimates (lower panel). We can see from the scatter plots how well the radiance model predicts the μ_ϕ as validated with the high resolution lidar measurements, with an $R^2 = 0.864$. Note that the two maps in the upper panels have the same color scale and show the same intensity trend. For this radiance acquisition the Sun's azimuth angle was 204° clockwise, coming from the south-west direction as can clearly be seen in the lidar map. Our radiance estimates show the same trend, with the highest μ_ϕ intensity coming from the south-west direction, and the lowest intensity exactly behind it, coming from the north-east.

For completeness, we also show reflectance retrievals over Beckman Auditorium's roof to illustrate the importance of leveraging the effect of the μ_ϕ variable in the forward model. Fig. 7 shows a comparison between our reflectance retrieval which solves also for μ_ϕ (panels A and C), compared to the same correction but when assigning a constant value based on the top of atmosphere solar zenith angle (panels B and D).

4.2. Validation over Valencia

The Valencia site is a rugged terrain area near Santa Clarita, California, where radiance measurements were acquired by AVIRIS-NG on September 10th 2016. We conducted two separate experiments over two different regions in the scene (Fig. 8), simulating typical high spatial resolution airborne measurements (green polygon), and typical moderate resolution orbital data (red polygon).

4.2.1. High resolution airborne experiment

In this experiment, we evaluated the suitability and capacity of our radiance based μ_ϕ estimates for airborne type spatial resolution. The region of the Valencia site is characterized by highly rugged terrain, north and south facing slopes, and mostly natural surfaces of soils, dry vegetation, and spare trees (Fig. 9).

We compared the radiance μ_ϕ estimates to three datasets: a high resolution lidar-based digital surface model (DSM), a high resolution lidar-based digital elevation model (DEM), and the SRTM DEM. To calculate the lidar based DSM, we acquired the raw point cloud measured by the lidar instrument and processed it minimally, only removing outlier points, before rasterizing the remainder to produce the DSM elevation dataset. The lidar DEM was precalculated by the USGS from the same point cloud measurements, and underwent removal of non-ground points from the cloud, followed by rasterization and smoothing

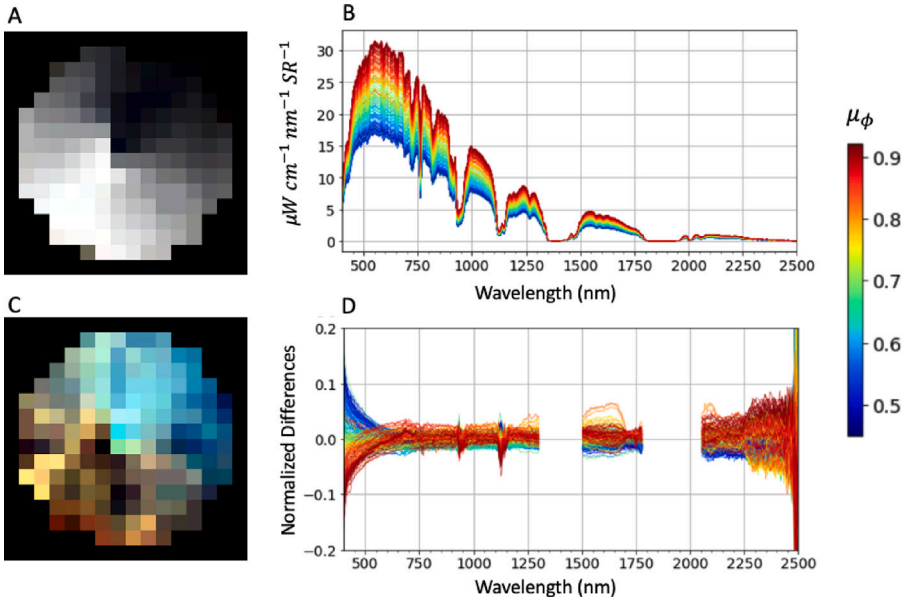

Fig. 5. The μ_ϕ variable has both a magnitude and a spectral shape effect on the measured radiance. Panel A shows a true color image from the radiance measurements, with individual spectra plotted in panel B, illustrating the magnitude effect. Panel C shows normalized differences in radiance, in true color, with the normalized spectra plotted in panel D, illustrating the spectral shape effect. Spectra in panels B and D are colored by the appropriate lidar-estimated μ_ϕ value. True color images in panels A and C are plotted with a linear min–max stretch.

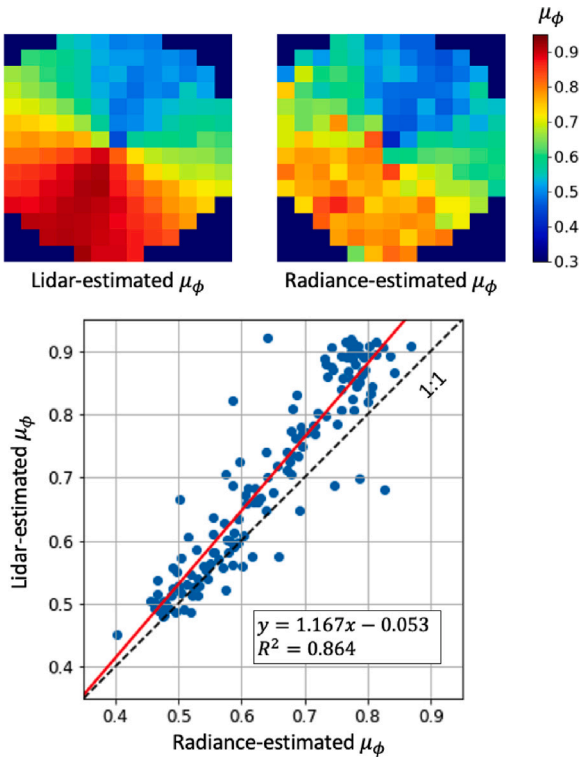

Fig. 6. Comparison between the lidar-estimated μ_ϕ map (upper left) to the radiance-estimated μ_ϕ map (upper right) for 160 pixels over Beckman Auditorium's roof. The lower panel shows a scatter plot for the pixel values above, with an $R^2 = 0.864$ and small bias.

of the result, producing the 1 m DEM USGS product. To match the radiance' GSD of 1.8 m, we downscaled the lidar datasets using pixel aggregation resampling, and calculated μ_ϕ according to Section 3.4. The SRTM dataset was processed to recover μ_ϕ using the same kernel method in its original 30 m resolution, before being upscaled to 1.8 m using bilinear interpolation resampling. Fig. 10 shows the four μ_ϕ datasets calculated according to the above description.

In Fig. 10, we can see excellent visual agreement between the radiance and lidar μ_ϕ estimates. Using only radiance measurements and an appropriate physical model this approach produced high accuracy estimates of the μ_ϕ parameter. Note the difference between the DSM (panel B) to the DEM (panel C), where the former shows more surface texture than the latter. The radiance estimates (panel A) appear to capture more texture than the DEM, but that texture is not aligned with the DSM map.

To numerically quantify the agreement between our radiance and the two lidar estimates, we plotted the values for all pixels in the map and calculate their correlation (Fig. 11). Surprisingly, the radiance estimates show higher correlation with the DEM map and not the DSM.

4.2.2. Orbital resolution experiment

Existing orbital imaging spectrometers such as PRISMA, EnMAP and EMIT, are observing Earth from a low Earth orbit of 400–700 km, producing radiance measurements with 30–60 m GSD. To evaluate our model performance in these conditions, we resampled all datasets to 30 m and applied the following processing. The radiance measurements were downscaled to 30 m using pixel aggregation, and our retrieval model was applied to the downscaled dataset. We produced a μ_ϕ map at 30 m based on the lidar USGS DEM by first calculating it at high resolution before downscaling the results using pixel aggregation. The SRTM data was processed at its original resolution of 30 m.

Fig. 12 shows the results of this analysis, exposing large variations between the three datasets. Whereas the radiance-based estimates show significant amount of sharp surface features, the DEM-based image seems to capture only the general shape of the scene. In contrast to the sharp features showed by both the radiance-based and the DEM-based images, SRTM produces a much more spatially smooth μ_ϕ map. Moreover, as in the airborne experiment, it seems that the radiance-based retrieval is underestimating μ_ϕ compared to the DEM, and that SRTM overestimates the μ_ϕ value.

4.2.3. Error analysis

The results presented above discuss two experiments, airborne and orbital. In the airborne experiment the radiance measurements are at 1.8 m GSD, the lidar measurements are at a nominal finer resolution but resampled to a coarser grid, and the SRTM dataset is at a much coarser resolution and is upsampled. In the orbital experiment, the SRTM dataset is at its nominal 30 m GSD resolution, and the radiance and DEM are both resampled to the coarse orbital projection using pixel aggregation. To evaluate the errors in these estimates, we compare the error distributions for each experiment. We define the μ_ϕ error as the difference between a μ_ϕ value calculated based on radiance, or the value based on the SRTM dataset, versus the USGS DEM μ_ϕ maps (Fig. 13).

The error distribution plots in Fig. 13 show a clear reduction of μ_ϕ error is obtained by using the radiance retrievals (versus SRTM) for airborne datasets, with weaker evidence for the orbital case. In both plots, we see a consistent underestimation of μ_ϕ by the radiance retrievals, and an overestimation by the SRTM quantities.

5. Discussion

In this work we demonstrated the new capability of extracting topographic information from radiance measurements with high accuracy. Our results indicate that this approach produces estimates with equivalent accuracy to airborne lidar, and has a key advantage of perfect spatial and temporal alignment. To our knowledge, this is the first work that demonstrates retrieval of topographic slope from at-sensor radiance. These estimates can be used for a unified atmospheric-topographic correction without the need for auxiliary datasets, producing better, more intrinsic, estimates of surface reflectance.

We validated our method's performance over two study sites in Southern California. The first is the Beckman Auditorium's roof on the Caltech campus in Pasadena, California. This target is homogeneous, smooth, and symmetric, and was used for an initial validation experiment to predict μ_ϕ over the roof's pixel and compare with high resolution lidar-based estimates. We found $R^2 = 0.864$ across 160 target pixels, with a slight underestimation that increases for high μ_ϕ values (Fig. 6). The second study site, Valencia, is a wild area with highly rugged terrain. A comparison between our radiance-based μ_ϕ estimates to the lidar DEM-based μ_ϕ estimates revealed $R^2 = 0.933$ across more than 40,000 px in the scene.

The ability to estimate μ_ϕ from radiance lies in the spectral effects of this variable on the measured signal. In Fig. 2 we show the spectral shape effect μ_ϕ has on modeled radiance using simulation. This experiment showed that the effect μ_ϕ has on at-sensor radiance is both a magnitude effect and a spectral shape (color) effect. This is significant because in the context of atmospheric correction, a magnitude shift effect on the radiance can be compensated by scaling the surface reflectance signature. Many biogeophysical models, such as mineral mapping, vegetation trait estimation and soil property mapping, normalize the reflectance curves in this way. Hence, if μ_ϕ had only a magnitude shift effect on the radiance, it would not cause significant errors in these applications. Instead, this analysis proved that μ_ϕ changes the color of the measured spectrum, and its effects cannot be compensated by scaling alone.

To further corroborate these findings we conducted a spectral analysis on the measured radiance over the Beckman Auditorium's roof target (Fig. 5). Panels A and B emphasize the magnitude change μ_ϕ

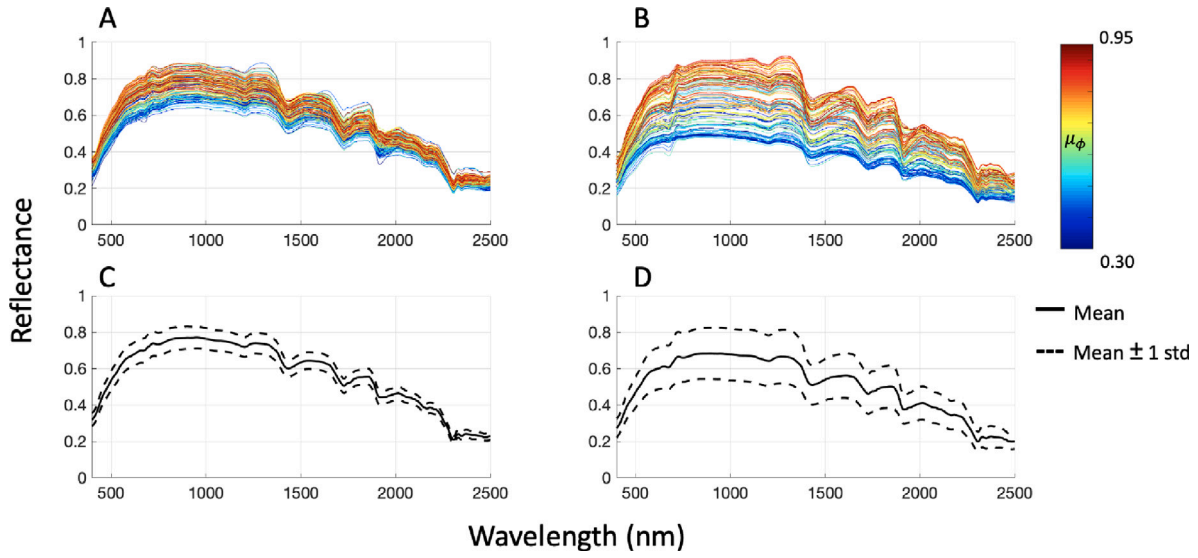

Fig. 7. Smaller errors in reflectance estimates are expected when solving for μ_ϕ (panel A), compared to assigning a constant value of the top of atmosphere solar zenith angle cosine. The spectra, colored by the retrieved μ_ϕ value show high dispersion when using the naive correction in panel B, suggesting the reflectance solution is correlated to μ_ϕ. In contrast, by solving for μ_ϕ the correlation is weaker as the reflectance estimates are more intrinsic to the roof's material.

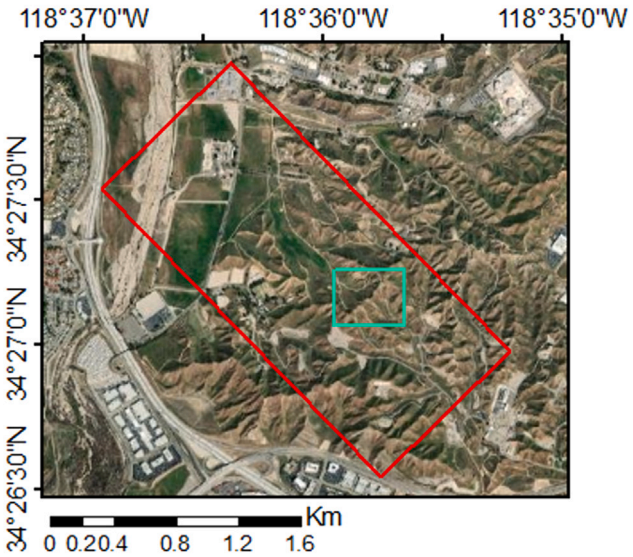

Fig. 8. The Valencia study site near Santa Clarita, California, featuring rugged hilly terrain and mostly natural surface cover. The green polygon area is used for typical high spatial resolution airborne measurements with 1.8 m GSD, whereas the red polygon is used for typical lower resolution orbital measurements with 30 m GSD.

has on the measured signal, while panels C and D emphasize the color change μ_ϕ causes in the radiance. Notably, panel C shows a true color RGB image of the normalized differences in the radiance pixels, clearly illustrating that the sun-facing side to the south-east is more yellow, and the non sun-facing side to the north-west is more blue, equivalent to the sun's and the sky's color balance. Finally, we prove that failing to compensate for μ_ϕ in atmospheric correction results in larger errors in the reflectance estimates (Fig. 7). In this experiment we calculated reflectance using our model while letting μ_ϕ be solved for within the optimization (panels A and C), or by assigning it a constant value, the same as the top of atmosphere solar zenith angle cosine (panels B and D). Our results clearly show that not accounting for μ_ϕ causes model discrepancy errors that change the reflectance solution. Moreover, this figure shows that the errors in reflectance are correlated to the μ_ϕ value, as the reflectance curve compensates for both the magnitude and the spectral shape effect of μ_ϕ.

The differences between radiance-based and lidar-based μ_ϕ estimates are critical to understand. In the Valencia study area we first evaluated our approach for a typical airborne resolution, with AVIRIS-NG radiance datasets at 1.8 m GSD. We compared our estimates against two lidar-derived elevation maps, a digital elevation model (DEM) and a digital surface model (DSM). Our initial expectation was that the radiance-based retrievals would better align with the surface model, not the elevation model, because the former retains the influence of surface features as observed by the radiance measurement, while in the latter those are removed. Our results show high correlation between the radiance-based estimates to both the DEM and DSM, with a slight advantage to the DEM-based μ_ϕ maps. The reason for this difference in correlation is unknown, although we postulate that most errors in the DSM-based μ_ϕ maps could be attributed to the DSM noise and the sensitivity of the μ_ϕ calculation to it.

Finally, we evaluate the capacity of this radiance based μ_ϕ retrieval for typical orbital measurements of moderate resolution (30 m GSD). A visual comparison in Fig. 12 clearly shows how the SRTM estimate strongly smooths the μ_ϕ map compared with both the radiance and lidar DEM based μ_ϕ maps. In Fig. 13 we see that μ_ϕ errors have similar magnitudes in both SRTM and radiance estimates, with SRTM overestimating and the radiance underestimating μ_ϕ. We argue that while the overestimating from SRTM is due to retrieval errors originating from the low resolution of these measurements, the underestimated μ_ϕ values from the radiance measurements might actually reflect better fidelity compared to the lidar DEM μ_ϕ maps. This topic is discussed further in Section 5.2.

5.1. Advantages

The key advantage of the presented approach over its pre-existing alternative is a perfect temporal and spatial alignment between μ_ϕ and the radiance that appears in the forward model. This ensures internal consistency of all modeled variables. With the conventional alternative of an external elevation dataset, it is very challenging to avoid systematic mismatches and resulting inversion errors.

A temporal gap between elevation and radiance measurements will expose the inversion to errors due to surface elevation changes in the

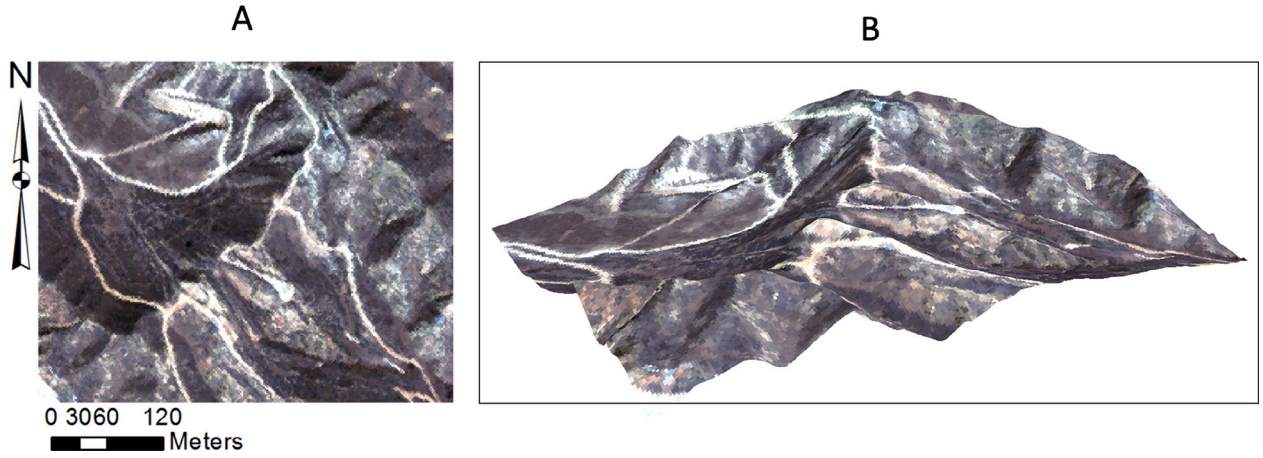

Fig. 9. The Valencia study site, situated near Santa-Clarita, California, shows natural surface cover with mostly dry vegetation, sparse trees, and bright soil paths (panel A). The site's highly rugged terrain shows north and south facing slopes (panel B), resulting in significant topographic effects.

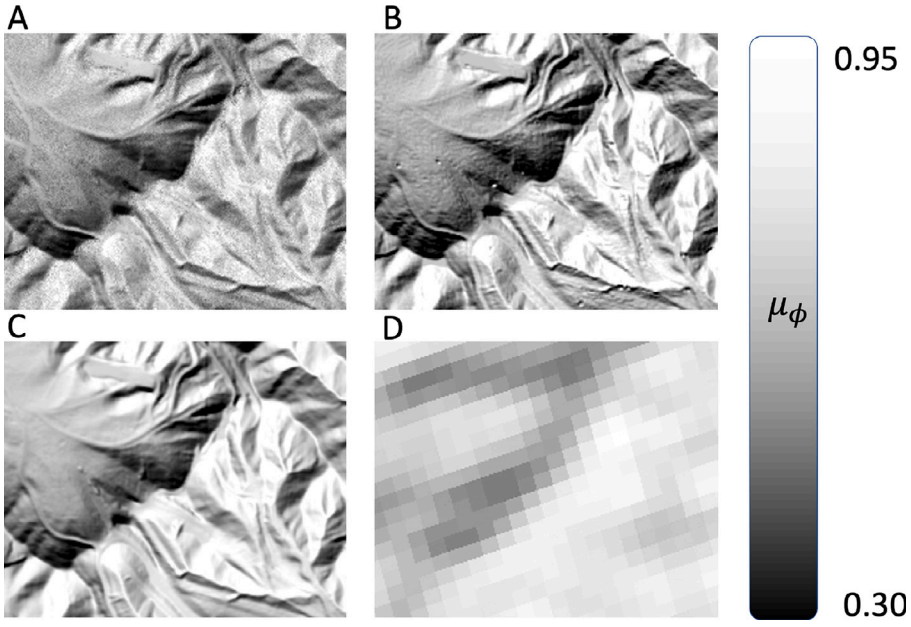

Fig. 10. High resolution (1.8 m GSD) μ_ϕ estimates derived from radiance (panel A), lidar-based digital surface model elevation map (panel B), lidar-based digital elevation model elevation map (panel C) and the NASA DEM elevation map (panel C).

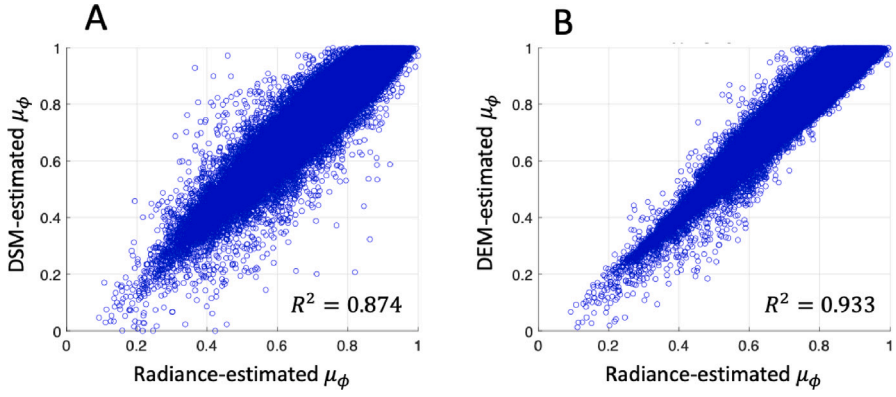

Fig. 11. Radiance-estimated vs. lidar-estimated μ_ϕ, where the lidar elevations come from a digital surface model (panel A), and a digital elevation model (panel B), within the Valencia study site.

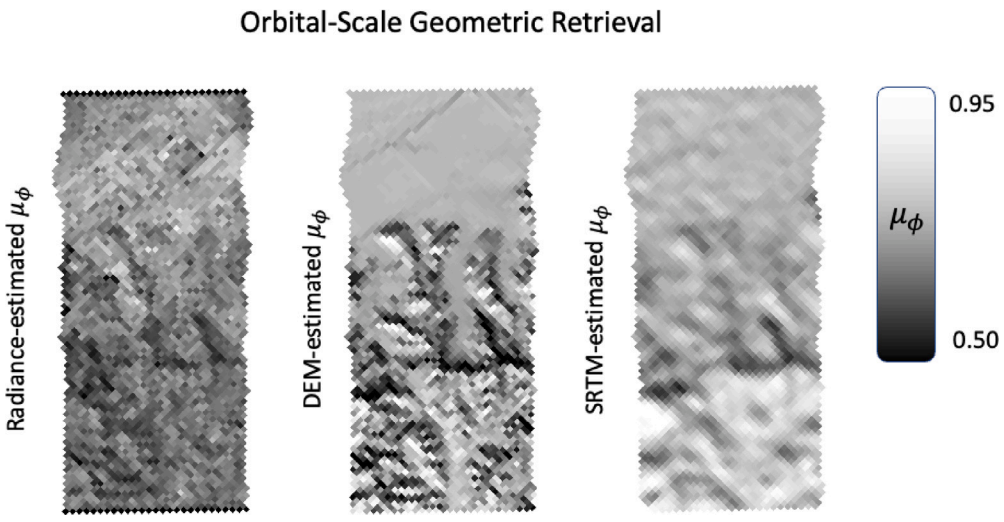

Fig. 12. For a typical Low Earth Orbit (400–700 km) instrument resolution of 30 m GSD, a comparison between the radiance-based (left), DEM-based (center), and SRTM-based (right) estimates of μ_ϕ, shows large variations over an extended region at the Valencia site. With the radiance-based estimates showing lower overall values but more surface features, they better capture sharp spatial variation compared to SRTM. Whereas the radiance estimates are calculated per-pixel, and the DEM is aggregated from a much higher resolution, only SRTM has a spatial bias in this resolution due to the use of a 3 × 3 kernel for the μ_ϕ calculation.

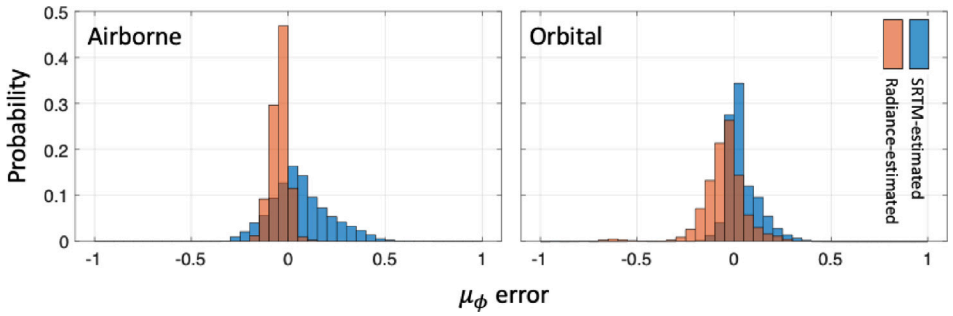

Fig. 13. A comparison between SRTM and radiance estimate of μ_ϕ to lidar-based digital elevation model μ_ϕ estimates. The left panel shows the results for a typical airborne resolution (1.8 m GSD), while the right panel shows the results for a typical orbital moderate resolution (30 m GSD).

intervening time. Many applications such as snow and ice mapping, vegetation traits estimation, and mineral mapping in arid areas show seasonal variations in the texture of the surface features. Depending on the temporal gap, changes in the actual topography might occur, such as in regions of volcanic activity, mud slides, and deforestation. The radiance-based model produces topographic estimates concurrent with the radiance, eliminating these confusing factors.

Using an auxiliary elevation map to derive μ_ϕ estimates also introduces spatial misalignment relative to observed radiances, resulting in uncertainties in the coregistered datasets. Spatial misalignment could be caused by several factors. First, differences in the original resolution of the products, especially if the elevation map has lower resolution than the radiance, would result in interpolation error in the combined product. Second, even if the elevation map has higher resolution than the radiance, differences in projection and coordinate system can cause the end product to be inaccurate. These systematic realities require a specialized processing of the elevation map to fit the radiance exactly, a process that requires validation and manual tuning. Third, differences in observation angle between the instrument measuring elevation and the one measuring radiance would mean that the surface map would be slightly shifted.

5.2. Defining μ_ϕ

Previously, the variable known as μ_ϕ was meant to account for the angle between the pixel's normal direction and the solar direction, and used to scale the direct flux based on this effect. In our model, this variable is a free parameter and will be affected not only by the overall average angle of the surface under a given pixel, but by any physical phenomenon that leads to a scaling of the direct flux on the surface area of the pixel visible to the instrument such as due to sub-pixel texture. Traditionally, within-pixel texture and shadows are treated by bidirectional reflectance distribution function (BRDF) models (Hapke, 2012). Most BRDF models have a geometric scattering component and a volume scattering component (Roujean et al., 1992) where the former accounts for textural shadows. In Fig. 10 note how the salt-and-pepper texture in the radiance retrieval is dissimilar to both the lidar-based DEM and DSM. This is later corroborated in Fig. 11 where the radiance estimates are consistently lower than the DEM and DSM μ_ϕ values. We postulate that the reason for this effect is not noise, but is due to the model's tendency to compensate not only for the macro texture, i.e., the average angle of the surface under a pixel to the solar direction, but also for its micro texture — within-pixel topography, surface feature texture, and within-pixel shadows.

Hence, the question of which μ_ϕ value to use, a purely elevation-derived one, or the radiance-derived one, is important. To answer this question, we must define the reflectance quantity we seek to provide as a product to be used for down stream analysis by biogeophysical models. An elevation-based μ_ϕ describes the reflectance of the pixel as if it were a hypothetical quadrilateral surface resting on the terrain. The resulting apparent reflectance would be influenced by the internal cast shadows of sub-pixel objects, an effect that would vary as a function of observation and illumination angles. Deriving μ_ϕ from digital elevation models would thus be appropriate for analysts who want to separate

atmospheric correction at the pixel scale from sub-pixel geometry, bookkeeping the latter as BRDF. This is the most common approach in recent ecological applications such as (Queally et al., 2022). Alternatively, estimating μ_ϕ from radiance leads to a reflectance estimate which may be more invariant to observation geometry. In the case where the materials in a pixel are Lambertian, and we consider only single-scattering optical paths, the μ_ϕ retrieval accounts for the variable solid angles subtended by illuminated and shadowed surfaces, leading to an estimate of the reflectance of the quadrilateral without its interior cast shadows. Even in cases where the materials are not Lambertian, as in the case of snow, retrieving the apparent μ_ϕ from radiance may result in reflectance estimates that are more invariant to observing geometry. The applicability of centimeter-scale, material-specific BRDF models to the de-shadowed reflectance estimates is a topic deserving further study.

5.3. Future work

In future work, we plan to incorporate BRDF models directly into the radiance equation. This would potentially allow us to disentangle micro and macro texture effects from the radiance measurements, and better estimate intrinsic reflectance for the surfaces under each pixel.

We also plan to further develop the unmixing approach presented in this work and estimate the underlying endmember reflectance signature to be used by a biogeophysical model. This would make sure that the application-relevant endmember reflectance signature is used, in contrast to applying a biogeophysical model built on pure endmember samples on multi-endmember mixture.

Finally, we plan to extend the applicability of this model to additional surface types such as snow and ice surfaces, arid deserts, and dense vegetation, as well as to evaluate the applicability of this approach to lower spectral resolution instruments.

6. Conclusions

In this work, we demonstrated the capacity to retrieve topographic variables strictly from radiance measurements. Our results show high accuracy when compared to high-resolution lidar datasets, and outperform the globally available SRTM. To our knowledge, this is the first work showing this capacity. We argue that the use of radiance-based topographic variables for atmospheric and topographic correction is significantly better than using auxiliary datasets. We postulate that this approach would be well suited for global imaging spectroscopy measurements such as those from the upcoming SBG mission.

CRediT authorship contribution statement

Nimrod Carmon: Conceptualization, Methodology, Software, Validation, Formal analysis, Investigation, Data curation, Writing – original draft, Writing – review & editing, Visualization, Funding acquisition. **Alexander Berk:** Conceptualization, Methodology, Formal analysis, Investigation, Writing – review & editing. **Niklas Bohn:** Methodology, Formal analysis, Investigation, Writing – original draft. **Phillip G. Brodrick:** Validation, Formal analysis, Investigation. **Jeff Dozier:** Formal analysis. **Margaret Johnson:** Methodology, Formal analysis, Writing – review & editing. **Charles E. Miller:** Validation, Resources, Writing – review & editing, Visualization. **David R. Thompson:** Software, Formal analysis, Investigation, Resources, Data curation, Writing – review & editing. **Michael Turmon:** Methodology, Formal analysis, Visualization, Project administration, Funding acquisition. **Charles M. Bachmann:** Methodology, Formal analysis, Writing – review & editing. **Robert O. Green:** Resources, Data curation, Supervision, Funding acquisition. **Regina Eckert:** Methodology, Investigation. **Elliott Liggett:** Validation, Investigation. **Hai Nguyen:** Methodology, Formal analysis. **Francisco Ochoa:** Formal analysis, Data curation. **Gregory S. Okin:** Formal analysis, Data curation, Writing – review & editing. **Rory Samuels:** Methodology. **David Schimel:** Formal analysis, Resources, Funding acquisition. **Joon Jin Song:** Methodology. **Jouni Susiluoto:** Methodology, Formal analysis.

Declaration of competing interest

The authors declare that they have no known competing financial interests or personal relationships that could have appeared to influence the work reported in this paper.

Data availability

Data will be made available on request.

Acknowledgments

We acknowledge and are thankful for the support of the Jet Propulsion Laboratory Research and Technology Development Program, and the NASA Land Cover and Land Use Change (LCLUC) program. We are thankful for the AVIRIS-NG instrument and Science Data System teams who ensured the high quality of the data used in this work. The research was carried out at the Jet Propulsion Laboratory, California Institute of Technology, under a contract with the National Aeronautics and Space Administration (80NM0018D0004).

References

Carmon, N., Berk, A., Bohn, N., Brodrick, P.G., Kalashnikova, O., Nguyen, H., Thompson, D.R., Turmon, M., 2022. Unified topographic and atmospheric correction for remote imaging spectroscopy. Front. Remote Sens. 3, 916155. http://dx.doi.org/10.3389/frsen.2022.916155.

Carmon, N., Thompson, D.R., Bohn, N., Susiluoto, J., Turmon, M., Brodrick, P.G., Connelly, D.S., Braverman, A., Cawse-Nicholson, K., Green, R.O., et al., 2020. Uncertainty quantification for a global imaging spectroscopy surface composition investigation. Remote Sens. Environ. 251, 112038. http://dx.doi.org/10.1016/j.rse.2020.112038.

Cawse-Nicholson, K., Townsend, P.A., Schimel, D., Assiri, A.M., Blake, P.L., Buongiorno, M.F., Campbell, P., Carmon, N., Casey, K.A., Correa-Pabón, R.E., et al., 2021. NASA's surface biology and geology designated observable: A perspective on surface imaging algorithms. Remote Sens. Environ. 257, 112349. http://dx.doi.org/10.1016/j.rse.2021.112349.

Chapman, J.W., Thompson, D.R., Helmlinger, M.C., Bue, B.D., Green, R.O., Eastwood, M.L., Geier, S., Olson-Duvall, W., Lundeen, S.R., 2019. Spectral and radiometric calibration of the next generation airborne visible infrared spectrometer (AVIRIS-NG). Remote Sens. 11 (18), 2129. http://dx.doi.org/10.3390/rs11182129.

Clark, R.N., Rencz, A.N., 1999. Spectroscopy of rocks and minerals, and principles of spectroscopy. Manual Remote Sens. 3 (11), 3–58.

Cogliati, S., Sarti, F., Chiarantini, L., Cosi, M., Lorusso, R., Lopinto, E., Miglietta, F., Genesio, L., Guanter, L., Damm, A., et al., 2021. The PRISMA imaging spectroscopy mission: Overview and first performance analysis. Remote Sens. Environ. 262, 112499. http://dx.doi.org/10.1016/j.rse.2021.112499.

Connelly, D.S., Thompson, D.R., Mahowald, N.M., Li, L., Carmon, N., Okin, G.S., Green, R.O., 2021. The EMIT mission information yield for mineral dust radiative forcing. Remote Sens. Environ. 258, 112380. http://dx.doi.org/10.1016/j.rse.2021.112380.

Doxani, G., Vermote, E., Roger, J.-C., Gascon, F., Adriaensen, S., Frantz, D., Hagolle, O., Hollstein, A., Kirches, G., Li, F., et al., 2018. Atmospheric correction inter-comparison exercise. Remote Sens. 10 (2), 352. http://dx.doi.org/10.3390/rs10020352.

Dozier, J., 2021. Revisiting topographic horizons in the era of big data and parallel computing. IEEE Geosci. Remote Sens. Lett. 19, 1–5. http://dx.doi.org/10.1109/LGRS.2021.3125278.

Dozier, J., Bair, E.H., Baskaran, L., Brodrick, P.G., Carmon, N., Kokaly, R.F., Miller, C.E., Miner, K., Painter, T.H., Thompson, D.R., 2022. Error and uncertainty degrade topographic corrections of remotely sensed data. JGR Biogeosci. http://dx.doi.org/10.1029/2022JG007147.

Dozier, J., Frew, J., 1990. Rapid calculation of terrain parameters for radiation modeling from digital elevation data. IEEE Trans. Geosci. Remote Sens. 28 (5), 963–969. http://dx.doi.org/10.1109/36.58986.

Gao, B.-C., Montes, M.J., Davis, C.O., Goetz, A.F., 2009. Atmospheric correction algorithms for hyperspectral remote sensing data of land and ocean. Remote Sens. Environ. 113, S17–S24. http://dx.doi.org/10.1016/j.rse.2007.12.015.

Green, R.O., Eastwood, M.L., Sarture, C.M., Chrien, T.G., Aronsson, M., Chippendale, B.J., Faust, J.A., Pavri, B.E., Chovit, C.J., Solis, M., et al., 1998. Imaging spectroscopy and the airborne visible/infrared imaging spectrometer (AVIRIS). Remote Sens. Environ. 65 (3), 227–248. http://dx.doi.org/10.1016/S0034-4257(98)00064-9.

Guanter, L., Kaufmann, H., Segl, K., Foerster, S., Rogass, C., Chabrillat, S., Kuester, T., Hollstein, A., Rossner, G., Chlebek, C., et al., 2015. The EnMAP spaceborne imaging spectroscopy mission for earth observation. Remote Sens. 7 (7), 8830–8857. http://dx.doi.org/10.3390/rs70708830.

Hapke, B., 2012. Theory of Reflectance and Emittance Spectroscopy. Cambridge University Press.

Jia, W., Pang, Y., Tortini, R., Schläpfer, D., Li, Z., Roujean, J.-L., 2020. A kernel-driven BRDF approach to correct airborne hyperspectral imagery over forested areas with rugged topography. Remote Sens. 12 (3), 432. http://dx.doi.org/10.3390/rs12030432.

JPL, N., 2020. NASADEM merged DEM global 1 arc second V001 [data set]. http://dx.doi.org/10.5067/MEaSUREs/NASADEM/NASADEM_HGT.001, URL https://lpdaac.usgs.gov/products/nasadem_hgtv001/.

Miller, C.J., 2002. Performance assessment of ACORN atmospheric correction algorithm. In: Algorithms and Technologies for Multispectral, Hyperspectral, and Ultraspectral Imagery VIII. 4725, SPIE, pp. 438–449. http://dx.doi.org/10.1117/12.478777.

Nguyen, H., Cressie, N., Braverman, A., 2012. Spatial statistical data fusion for remote sensing applications. J. Amer. Statist. Assoc. 107 (499), 1004–1018. http://dx.doi.org/10.1080/01621459.2012.694717.

Perkins, T., Adler-Golden, S., Matthew, M., Berk, A., Anderson, G., Gardner, J., Felde, G., 2005. Retrieval of atmospheric properties from hyper and multispectral imagery with the FLAASH atmospheric correction algorithm. In: Remote Sensing of Clouds and the Atmosphere X, Vol. 5979. SPIE, pp. 114–124. http://dx.doi.org/10.1117/12.626526.

Queally, N., Ye, Z., Zheng, T., Chlus, A., Schneider, F., Pavlick, R.P., Townsend, P.A., 2022. FlexBRDF: A flexible BRDF correction for grouped processing of airborne imaging spectroscopy flightlines. J. Geophys. Res.: Biogeosci. 127 (1), e2021JG006622. http://dx.doi.org/10.1029/2021JG006622.

Raiho, A., Cawse-Nicholson, K., Chlus, A., Dozier, J., Gierach, M.M., Miner, K., Serbin, S.P., Schimel, D., Schneider, F., Shiklomanov, A.N., et al., 2022. Exploring mission design for imaging spectroscopy retrievals for land and aquatic ecosystems. Earth Space Sci. Open Arch. 21. http://dx.doi.org/10.1002/essoar.10510949.1.

Rast, M., Nieke, J., Adams, J., Isola, C., Gascon, F., 2021. Copernicus hyperspectral imaging mission for the environment (chime). In: 2021 IEEE International Geoscience and Remote Sensing Symposium IGARSS. IEEE, pp. 108–111.

Richter, R., Schläpfer, D., 2019. Atmospheric and topographic correction (ATCOR theoretical background document).

Rodgers, C.D., 2000. Inverse Methods for Atmospheric Sounding: Theory and Practice, Vol. 2. World scientific.

Roujean, J.-L., Leroy, M., Deschamps, P.-Y., 1992. A bidirectional reflectance model of the Earth's surface for the correction of remote sensing data. J. Geophys. Res.: Atmos. 97 (D18), 20455–20468. http://dx.doi.org/10.1029/92JD01411.

Shimabukuro, Y.E., Smith, J.A., 1991. The least-squares mixing models to generate fraction images derived from remote sensing multispectral data. IEEE Trans. Geosci. Remote Sens. 29 (1), 16–20.

Soenen, S.A., Peddle, D.R., Coburn, C.A., 2005. SCS+ C: A modified sun-canopy-sensor topographic correction in forested terrain. IEEE Trans. Geosci. Remote Sens. 43 (9), 2148–2159. http://dx.doi.org/10.1109/TGRS.2005.852480.

Stavros, E.N., Chrone, J., Cawse-Nicholson, K., Freeman, A., Glenn, N.F., Guild, L., Kokaly, R., Lee, C., Luvall, J., Pavlick, R., et al., 2022. Designing an observing system to study the surface biology and geology (SBG) of the earth in the 2020s. J. Geophys. Res.: Biogeosci. e2021JG006471. http://dx.doi.org/10.1029/2021JG006471.

Thompson, D.R., Braverman, A., Brodrick, P.G., Candela, A., Carmon, N., Clark, R.N., Connelly, D., Green, R.O., Kokaly, R.F., Li, L., et al., 2020a. Quantifying uncertainty for remote spectroscopy of surface composition. Remote Sens. Environ. 247, 111898. http://dx.doi.org/10.1016/j.rse.2020.111898.

Thompson, D.R., Gao, B.-C., Green, R.O., Roberts, D.A., Dennison, P.E., Lundeen, S.R., 2015. Atmospheric correction for global mapping spectroscopy: ATREM advances for the HyspIRI preparatory campaign. Remote Sens. Environ. 167, 64–77. http://dx.doi.org/10.1016/j.rse.2015.02.010.

Thompson, D.R., Natraj, V., Green, R.O., Helmlinger, M.C., Gao, B.-C., Eastwood, M.L., 2018. Optimal estimation for imaging spectrometer atmospheric correction. Remote Sens. Environ. 216, 355–373. http://dx.doi.org/10.1016/j.rse.2018.07.003.

Thompson, D.R., Schimel, D.S., Poulter, B., Brosnan, I., Hook, S.J., Green, R.O., Glenn, N., Guild, L., Henn, C., Cawse-Nicholson, K., et al., 2020b. NASA's surface biology and geology concept study: Status and next steps. In: IGARSS 2020-2020 IEEE International Geoscience and Remote Sensing Symposium. IEEE, pp. 3269–3271. http://dx.doi.org/10.1109/IGARSS39084.2020.9323295.

Wang, J., White, K., Robinson, G.J., 2000. Estimating surface net solar radiation by use of Landsat-5 TM and digital elevation models. Int. J. Remote Sens. 21 (1), 31–43. http://dx.doi.org/10.1080/014311600210975.